ACS Partner Journal

CHEM & BIO ENGINEERING

pubs.acs.org/ChemBioEng

Article

Type III Collagen Promotes Pseudopodium-Driven Cell Migration

Ruiwen Fu,[#] Kuangzheng Zhu,[#] Zhouyang Li,[#] Liqun Lei,[#] Ming Li,[*] Xuye Lang,[*] and Yuan Yao[*]

Cite This: *Chem Bio Eng.* 2025, 2, 97−109

Read Online

ACCESS | Metrics & More | Article Recommendations | Supporting Information

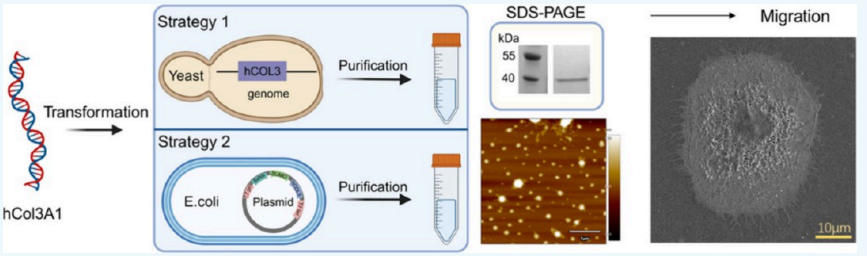

ABSTRACT: The extracellular matrix (ECM), particularly collagen, is acknowledged for its significant impact on cell migration. However, the detailed mechanisms through which it influences pseudopodium formation and cell motility are not yet fully understood. This study delves into the impact of recombinant human type III collagen (hCOL3) on cell migration, specifically focusing on the dynamics of pseudopodia and their contribution to cell motility. The research evaluates the impact of a fragmented form of hCOL3, engineered for the study, on cell motility and pseudopodium behavior using both single-cell and collective-cell migration assays. The results demonstrate that hCOL3 promotes cell migration velocity, augments the effective diffusion coefficient, and enhances directionality in both single-cell and collective migration contexts. Observations from scanning electron microscopy reveal that treatment with hCOL3 increases both the number and length of filopodia, which are crucial for cell migration and interaction with the ECM. The study suggests that hCOL3 facilitates a more targeted and rapid migration. The presence of an increased number of filopodia on surfaces treated with hCOL3 enhances the cell's ability to detect environmental cues and extent, thereby augmenting its migratory capacity. This discovery could potentially lead to greater efficiency in wound healing processes.

KEYWORDS: *hCOL3, Cell Migration, Dynamics, Pseudopodium, Filopodium*

1. INTRODUCTION

Cell migration plays a pivotal role in physiological processes such as embryonic development, tissue repair, and immune response.[1,2] Cells perceive and react to environmental stimuli, moving toward or away from these cues to carry out developmental morphogenesis, trigger immune responses, and facilitate tissue repair.[3,4] Dysregulation of cell migration can lead to severe physiological outcomes, including metastatic cancer,[5] autoimmune diseases,[6] and fibrosis.[7] Directed cell migration is underpinned by signal generation, perception, transduction, and conversion into asymmetric or polarized forces, primarily mediated by the cytoskeleton.[4]

Collagen, especially collagen I and collagen III, is crucial for cell survival, scar formation, disease progression, and recovery.[8] It has been shown to accelerate the closure of chronic wounds when used as a carrier for fibroblast growth factor (FGF).[9] Collagen's topological properties, such as fiber thickness and arrangement, provide directional cues for cell migration.[10−12] Modulating collagen network properties can affect network deformation, relaxation times, and migration persistence.[13] However, the cell responses to the collagen matrices as migration dynamics are underinvestigated.[14] Pseudopodia, as specialized cellular protrusions, are vital for cell migration, allowing cells to interact with the extracellular matrix (ECM). These structures, either lamellipodia or filopodia, contain a high concentration of new f-actin filaments upon activation, suggesting that actin polymerization powers pseudopodial extension.[15] Typically, initial cell adhesion to the ECM occurs via integrin receptors. When exposed to soluble factors, cells sense chemoattractants and enhance signaling pathways. This leads to actin polymerization and membrane protrusion toward the gradient.[16−18] The formation of adhesive contacts is also crucial for generating contractile forces and traction between the ECM and migrating cells.[19] Cell migration is a dynamic and multifaceted process that relies on the coordinated function of the cytoskeleton, adhesion molecules, and signaling pathways. Pseudopodium plays a critical role in this process, to probe and interact with the ECM, and thus dictate the trajectory of cell migration. In zebrafish embryos, primordial germ cells (PGCs) use filamentous protrusions to migrate toward the chemokine

Received: August 12, 2024
Revised: September 14, 2024
Accepted: September 15, 2024
Published: October 7, 2024

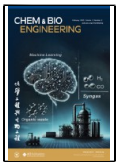

Cxcl12a.[20] The Cxcl12a signal activates IRSp53, promoting cell polarization and increasing the number of transient filopodia directed toward the gradient. These filopodia amplify the signal, leading to a localized increase in cellular pH and activation of Rac1.[21] Filopodia formation is critical for Cxcl12a-guided migration.[20] During wound healing, filopodia on migrating epithelial cell sheets is essential for effective binding and tissue pattern organization.[22,23] Thus, understanding the interplay between pseudopodium formation and function is crucial for an understanding of cell migration dynamics and is instrumental for advancing wound healing research.

Although collagen's role in cell migration is well-established, the specific influence of collagen on pseudopodium and subsequent impacts on cell motility has not been thoroughly investigated. This represents a great gap, addressing which could improve our comprehension of cell migration dynamics. Human type III collagen, essential for the structural integrity and mechanical support of various tissues, is known to facilitate cellular migration and motility, which are key to wound repair and tissue regeneration. However, the literature lacks a comprehensive, quantitative analysis of its influence on cell motility and pseudopodium formation. This study aims to address this gap by engineering a recombinant human type III collagen(hCOL3) to investigate its modulation of cell motility, pseudopodium formation, and migration dynamics.

2. MATERIALS AND METHODS

2.1. Design, Engineering, and Biosynthesis of hCOL3 Protein. Two specific gene fragments of hCOL3 were amplified. These fragments were then ligated through homologous recombination, culminating in the formation of a human type III collagen COL3A1 gene fragment. The designed COL3A1 sequence was biosynthesized by two expression systems, *Escherichia coli* (*E. coli*) ER2566 and *Kluyveromyces marxianus* (*K. marxianus*) CBS6556. For the *E. coli* system, the resultant polypeptide sequence was subsequently cloned into the pRSFDuet1 plasmid, which was engineered to include His-SUMO tags. This fusion yielded the construct His-SUMO-hCOL3-RSFD, enhancing the protein's solubility and facilitating downstream purification processes. The pRSFDuet1-based vectors were successfully transformed into chemically competent *E. coli* ER2566 cells. These cells were then plated on Luria−Bertani (LB) agar plates supplemented with 50 μg/mL kanamycin and incubated at 37 °C overnight. The following day, the strain was cultured in 20−2000 mL LB containing kanamycin (10 μL of a 100 mg/mL solution) at 37 °C with shaking at 220 rpm (rpm) until the optical density at 600 nm (OD600) reached 0.6. Subsequently, isopropyl β-D-1-thiogalactopyranoside (IPTG) was introduced to induce the expression of the recombinant protein. The cultures were then incubated for an additional 18 h at 20 °C with continuous agitation at 220 rpm. After incubation, cells were harvested by centrifugation and resuspended in a buffer containing 20 mM Tris-HCl, 20 mM imidazole, and 500 mM NaCl, adjusted to a pH of 8.0, with the aid of lysozyme. The resuspended solution underwent high-pressure homogenization at 800 bar using an AH-1500 (ATS) device to facilitate protein extraction. For the *K. marxianus* system, His-SUMO-hCOL3 was expressed by GPD promoter (pGPD), and the pGPD-hCOL3-His-tCYC1 expression cassette was integrated into XYL2 loci using CRISPR-Cas9 system. The sequence was amplified using specific primers derived from the His-Sumo-COL III plasmid (Supporting Information Table S1).

2.2. Protein Purification. For the collagen in *E. coli*, the purification process commenced with filtration through a 0.22 μm membrane. The resulting filtrate was then loaded onto a Ni-NTA affinity column (HUACHUN, 5 mL HiTrap). The target proteins were eluted using a high-imidazole buffer containing 20 mM Tris-HCl, 500 mM NaCl, and 500 mM imidazole, with the process managed on an AKTA protein purification system (AKTA pure 25, GE Healthcare). Subsequently, the protein was incubated with Ulp1 enzyme in a buffer comprising 20 mM Tris-HCl, 20 mM imidazole, 500 mM NaCl, and 2 M urea at 4 °C. The mixture was then reapplied to the Ni-NTA column, and the flow-through, containing the target proteins, was collected using the AKTA system. The purified protein solution was dialyzed against PBS buffer (pH 7.4, Gibco) for 24 h. The purity and identity of the resulting human type III collagen (hCOL3) were assessed using sodium dodecyl sulfate-polyacrylamide gel electrophoresis (SDS-PAGE, 4%−20%, GenScript) followed by Coomassie Brilliant Blue staining.

For the collagen in *K. marxianus* CBS6556, the engineered strain, harboring the collagen gene in the genome, was first cultivated in 3 mL of SD liquid medium for 16 h at 30 °C. The culture was then scaled up to 200 mL of the same medium and incubated for an additional 36 h at 25 °C, beginning with an initial optical density (OD) of 0.05. Cell disruption was performed using an ultrasonic cell crusher at 400W on ice, with a cycle of 3 s of sonication followed by a 7-s pause for a total of 30 min. The supernatant, containing the crude protein, was obtained by centrifugation at 12,000 rpm for 40 min. The protein was purified using an affinity chromatography column packed with Ni-Sepharose 6 Fast Flow, managed by the AKTA purification system (GE Healthcare, USA). The column was equilibrated with the low-imidazole buffer before the application of the crude protein solution. The target protein was eluted with a high-imidazole buffer (20 mM Tris-HCl, pH 8.0, 500 mM NaCl, 500 mM imidazole). The eluted protein was concentrated to 3 mL using an ultrafiltration centrifuge tube, and its purity was confirmed by sodium dodecyl sulfate-polyacrylamide gel electrophoresis (SDS-PAGE) analysis.

2.3. Atomic Force Microscopy. Atomic force microscopy (AFM) analysis was conducted using a Bruker Dimension FastScan Atomic Force Microscope. The samples were examined in the air under the ScanAsyst mode, employing a ScanAsyst-Air probe for optimal imaging. The preparation of the samples involved spin-coating a 20 μL aliquot of the protein solution onto pristine silicon wafers. Postcoating, the wafers were meticulously rinsed with deionized water to eliminate any residual salt ions. Following the rinsing process, the wafers were allowed to dry naturally at room temperature overnight before imaging.

2.4. Cell Proliferation Assay. In the study of cell proliferation, we utilized the EdU incorporation assay, employing a commercial kit (BeyoClick EdU Cell Proliferation Kit with Alexa Fluor 488, Beyotime, China). Initially, cells were seeded at a density of 5×10^4 cells per well in 96-well plates and cultivated in DMEM supplemented with hCOL3 for 24 h. They were then fixed with a 4% paraformaldehyde solution for 15 min and permeabilized using a 0.3% Triton X-100 solution for an additional 15 min. The cells were subjected to a click reaction mixture for 30 min at room temperature in the dark, followed by a 10 min incubation with Hoechst.

2.5. Cell Differentiation Assay and Real-Time PCR. We employed the method of collagen plating and coated 24-well plates with hCOL3. 300 μL of hCOL3 (6.4 mg/mL) were added to the well plates, left for 18h at room temperature for self-assembly, and incubated with DMEM complete medium for 2h in a 37 °C incubator. WB-F344 cells (2×10^5 cells/well) were seeded in the hCOL3-coated 24-well plates and cultured for 24 h. Cells were washed with PBS, and RNA was isolated using RNA isolation Total RNA Extraction Reagent (Vazyme), following standard protocol. To prepare cDNA, 500 ng RNA was prepared with gDNA wiper for 5 min, and cDNA was synthesized with HiScript II Q RT SuperMix for qPCR (Vazyme). Real-time PCR reactions contained cDNA (1:3 dilution), forward and reverse primers,[23] and Taq Pro Universal SYBR qPCR Master Mix(Table S2). Each sample was analyzed in triplicate (ABI Stepone plus, Thermo Fisher Scientific).

2.6. Immunofluorescence Imaging. Cells were seeded onto 14 mm diameter coverslips (Biosharp) housed within a 24-well plate. The coverslips were precoated with hCOL3 24 h before cell seeding, ensuring a uniform and stable extracellular matrix. Following cell seeding, the cells were fixed with a 4% paraformaldehyde (PFA) solution for 15 min and then permeabilized with a 0.5% Triton X-100 solution (Sangon Biotech, Shanghai, China). To prevent nonspecific binding, 5% bovine serum albumin (BSA, Sigma) was applied and incubated for 30 min. Subsequently, the cells were incubated with the

https://doi.org/10.1021/cbe.4c00133
Chem Bio Eng. 2025, 2, 97−109

primary antibody diluted to 1:1000 in 5% BSA at 4 °C overnight. On the subsequent day, after discarding the primary antibody, a secondary antibody diluted to 1:1000 in PBS was added to the wells and incubated at room temperature for 90 min. For cytoskeletal and nuclear staining, phalloidin (1:500, Sigma) and Hoechst (1:2000, Beyond) were applied following the secondary antibody incubation, with incubation periods of 120 and 15 min, respectively. After each incubation step, and before the subsequent step except for after blocking and before the primary antibody incubation, the fixed cells were washed twice with a 0.1% BSA solution in PBS for 5 min. The coverslips were then mounted using an antifade reagent (Sigma) and imaged using confocal microscopy with a 60×/1.5 NA objective lens (Olympus Fluoview FV3000). The *z*-step for *z*-stack scanning was set at 0.5 μm to capture the cellular structures in three dimensions.

2.7. Cell Migration Assay. For the assessment of single-cell migration, a range of 20,000 to 30,000 cells were plated onto 24-well plates that had been precoated with hCOL3 for 24 h before cell seeding. Live imaging was initiated the day following cell plating. In the context of wound-healing assays, silicone inserts from a specific manufacturer were placed within 24-well plates from Corning. Purified hCOL3, prepared as described in method 2.4, or phosphate-buffered saline (PBS), 60 μL in volume, was applied to each side of the silicone insert to coat for 24 h. After the removal of the fluid and subsequent washing with PBS, 60 μL of a cell suspension at a concentration of 1.5 to 2 million cells per milliliter was added to each side of the inset. The insert modules were removed the following day, and fresh culture medium was added to the wells in preparation for live imaging. All live imaging was conducted using a LionHeart automated live-cell imaging system equipped with a 10×/1.4 NA objective lens, under standard cell culture conditions (37 °C and 5% CO_2; complete culture medium). Imaging was performed at intervals of every 30 min.

2.8. Scanning electron microscope (SEM). Cells were seeded onto 14 mm diameter coverslips within a 24-well plate, with manual application of human collagen type III (hCOL3) as a coating, followed by culture for 24 h. After the medium was discarded, the cells were gently washed three times with PBS to remove any residual culture components. Subsequently, the cells were fixed using a 4% paraformaldehyde (PFA) solution for 30 min at room temperature to preserve their structure. Following fixation, the cells were again washed three times with PBS. The dehydration process involved sequential immersion of the samples in increasing concentrations of ethanol (10%, 30%, 50%, 70%, 90%, and 100%) for 10 min each, followed by a final 30 min soak in 100% ethanol to ensure complete dehydration. Once dehydrated, the samples were prepared for scanning electron microscopy by sputter-coating them with a thin layer of gold to enhance image contrast. The cellular morphology was then examined using a scanning electron microscope (Scios 2 DualBeam, Thermo Fisher Scientific).

2.9. Analysis of Cell Migration Dynamics. For each cell analyzed after cell migration assay (2.7), the (x,y) coordinates were recorded from t = 0 to the end of the experiment at every 30 min interval, using the Cell Tracking Plugin in ImageJ software. The raw data set of cell movement is finally presented as (n, k, x, y), where n is the ID of the cell analyzed, k is the order of frame through the time axis, following the arithmetic sequence $\{1, 2, 3, 4, ...\}$ at which the cell is analyzed, and (x, y) is the 2D coordinates. From this data set, the following physical quantities can be deduced:

$$t = \Delta t(k - 1) \tag{1}$$

where Δt = 0.5 h for all live cell imaging experiments in this research.

velocity vector of cell with ID n at time point t

$$\mathbf{v}(t)_n = \left(\frac{dx}{dt}, \frac{dy}{dt}\right)_n \tag{2}$$

acceleration vector of cell with ID n at time point t

$$\mathbf{a}(t)_n = \left(\frac{d^2x}{dt^2}, \frac{d^2y}{dt^2}\right)_n \tag{3}$$

therefore, the direction (angle) of the cell with ID n at time point t

$$\theta(t)_n = \arctan\left(\frac{dy}{dt} / \frac{dx}{dt}\right)_n \tag{4}$$

$\left(\frac{dx}{dt}, \frac{dy}{dt}\right)_n$ and $\left(\frac{d^2x}{dt^2}, \frac{d^2y}{dt^2}\right)_n$ are approximated by spline interpolating $x(t)_n$ and $y(t)_n$ with 0.25 h time interval.

Discrete travel length (distance) of cell with ID n between frame i and $i + 1$:

$$\Delta L_n = \sqrt{(x_{i+1} - x_i)^2 + (y_{i+1} - y_i)^2} \tag{5}$$

Length traveled by cell with ID n at time t (frame k) is therefore

$$L(t)_n = \int_0^t \sqrt{dx^2 + dy^2} \approx \sum_{i=1}^{k} \sqrt{(x_{i+1} - x_i)^2 + (y_{i+1} - y_i)^2} \tag{6}$$

expressed as the Riemann Integral.[24]

The Time Mean Speed of cell with ID n is therefore

$$\overline{v_n} = \frac{L(t_{\text{total}})_n}{t_{\text{total}}} \tag{7}$$

Squared displacement of cell with ID n at time t:

$$\mathbf{r}^2(t)_n \equiv (x(t)_n - x(0)_n)^2 + (y(t)_n - y(0)_n)^2 \tag{8}$$

The directionality ratio of a cell at time t is defined as[25]

$$d(t)_n = \frac{\sqrt{\mathbf{r}^2(t)_n}}{L(t)_n} \tag{9}$$

All cell mean variables (ensemble average) are defined as

$$\langle f(t)_n \rangle \equiv \frac{1}{n_{\text{total}}} \sum_{n=1}^{n_{\text{total}}} f(t)_n \tag{10}$$

including mean squared displacement (MSD).

MSD of single-cell movement is fitted using

$$\langle \mathbf{r}^2(t) \rangle = D_{\text{eff}}[t - \tau_p(1 - e^{-t/\tau_p})] \tag{11}$$

The ensemble average of lengths traveled by cell at time t is fitted using

$$\langle L(t) \rangle = Ut \tag{12}$$

To find a model that approximates the MSD of leading cells in wound healing movement, first assume that the gap of the wound is infinite. Due to the application of momentum field and close-to-unidirectional migration, it is to assume a superdiffusion or hyper-ballistic diffusion model:

$$\langle \mathbf{r}^2(t) \rangle = At^{\alpha} \tag{13}$$

where $\alpha > 1$ and A is a constant.

The rate at which $\langle \mathbf{r}^2(t) \rangle$ increases with respect to time is therefore

$$\frac{d}{dt}\langle \mathbf{r}^2(t) \rangle = \alpha A t^{\alpha - 1} \tag{14}$$

If the gap is finite, the increasing rate of MSD becomes limited when the movement is close **to wound closure**. In this case, assuming it is similar to the case of bacterial growth with limited nutrients, a limiting term $\left(1 - \frac{\langle \mathbf{r}^2(t) \rangle}{R_C^2}\right)$ is multiplied, where R_C^2 is a characteristic MSD, a constant parameter for the system:

https://doi.org/10.1021/cbe.4c00133
Chem Bio Eng. 2025, 2, 97−109

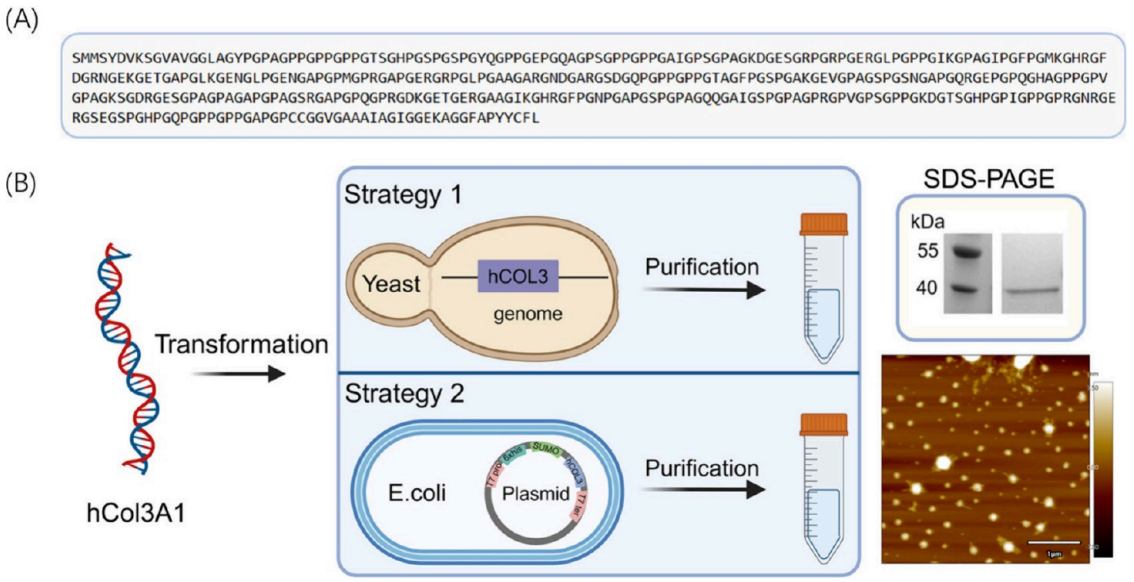

Figure 1. Design and biosynthesis of hCOL3. (A) Protein sequence of hCOL3. (B) Schematic illustration of hCOL3 biosynthesis by *E. coli* ER2566 and *K. marxianus* CBS6556 and self-assembly material by hCOL3 (AFM image).

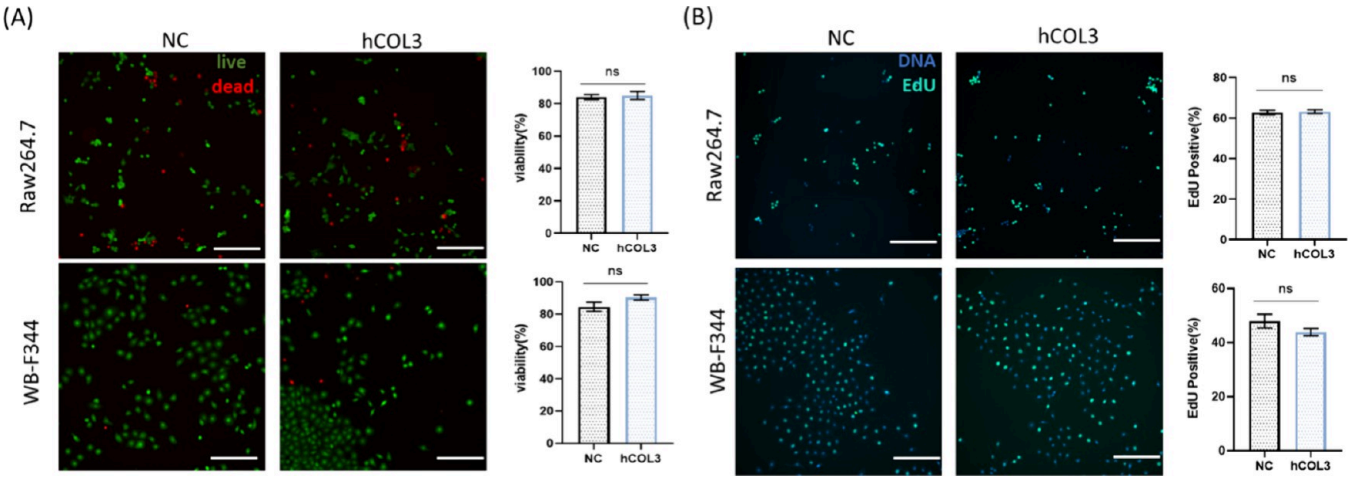

Figure 2. Cell viability and proliferation of hCOL3. (A) Viability assessed through staining with both calcein (green, live) and propidium Iodide (red, dead) on Raw264.7 and WB-F344 cells, respectively. The proportion of live cells among the total cells per frame is depicted in the bar graphs on the right. (B) Proliferation evaluated via EdU staining with green fluorescence on Raw264.7 and WB-F344 cells, respectively. The proportion of EdU-positive cells (proliferating cells) per frame is shown in the bar graphs on the right. Statistics in bar graph include greater than 6 frames per condition for both panels A and B. Scale bar = 200 μm for all images.

$$\frac{\mathrm{d}}{\mathrm{d}t}\langle \mathbf{r}^2(t)\rangle = \alpha A t^{\alpha-1}\left(1 - \frac{\langle \mathbf{r}^2(t)\rangle}{{R_\mathrm{C}}^2}\right) \tag{15}$$

Solving this differential equation, there is

$$\langle \mathbf{r}^2(t)\rangle = {R_\mathrm{C}}^2[1 - \mathrm{e}^{-At^\alpha/{R_\mathrm{C}}^2}] \tag{16}$$

Similarly, if it is assumed that the ensemble average length traveled by a cell takes the same form, then

$$\langle L(t)\rangle = L_\mathrm{C}[1 - \mathrm{e}^{-Bt^\gamma/L_\mathrm{C}}] \tag{17}$$

where L_C is characteristic length, and L_C, B, and γ are all constant parameters.

2.10. Geometric Quantity Evaluation. All 2D geometric quantities in this research were analyzed using ImageJ by specifying the contour of objects on $x-y$ plane. Objects on $x-y$ plane are either a z-project or a 3D-project of nuclei or cells from confocal microscopy. Projected area (A), perimeter (P), and aspect ratio can be directly measured with ImageJ when the contour is specified, while circularity is calculated as

$$c = \frac{4\pi A}{P^2} \tag{18}$$

The volume of nuclei is calculated by approximating a nuclei as a hemiellipsoid. Confocal microscopy images of nuclei are converted to a 3D project using ImageJ. The $x-y$ projected area of nuclei (equatorial area, A) and the radii of hemiellipsoid at z-direction (h) were both measured using ImageJ, denoted as h. The volume of nuclei is calculated as

$$V = \frac{2Ah}{3} \tag{19}$$

2.11. Cytoskeleton and Filopodium Analysis. z-projected confocal microscopy was utilized to analyze cells stained for actin and tubulin, focusing on the channels that highlight these cytoskeletal components. The analysis employed a filament sensor, which quantified filament length and orientation (angle) data, providing insights into the

https://doi.org/10.1021/cbe.4c00133
Chem Bio Eng. 2025, 2, 97−109

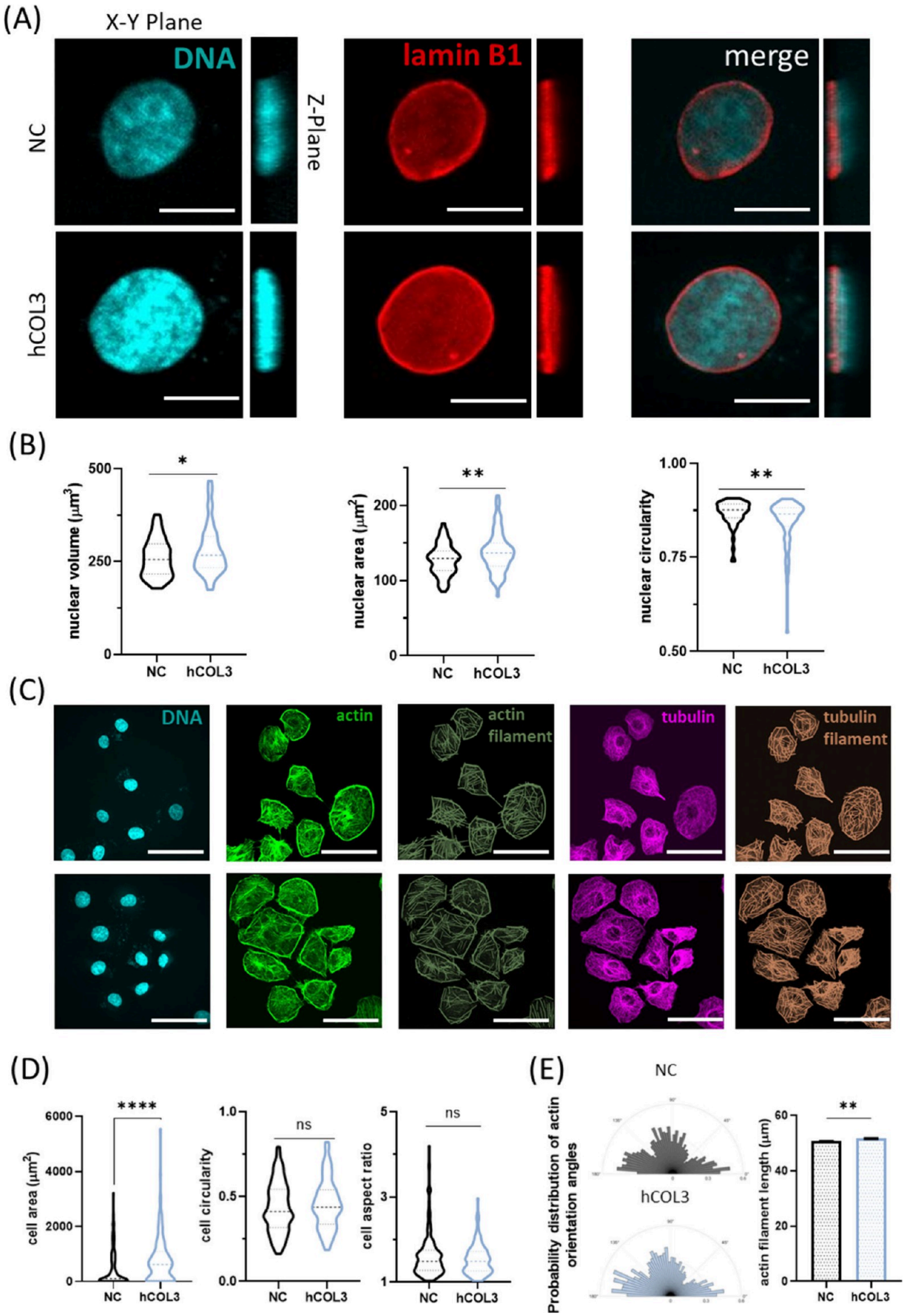

Figure 3. hCOL3 coating inducing morphological and cytoskeletal changes. (A) Confocal images depicting nuclei of WB-F344 cells plated on NC and hCOL3 conditions, respectively, with DNA and Lamin B1 (located at the inner shell of nuclei) displayed. Scale bar = 10 μm for all images. Images

https://doi.org/10.1021/cbe.4c00133
Chem Bio Eng. 2025, 2, 97−109

Figure 3. continued

across all dimensions share the same scale. (B) Violin plots illustrating statistics of morphological properties of cell nuclei plated on NC and hCOL3 conditions. (C) Confocal images of cells plated on NC and hCOL3 conditions, with DNA, actin, software-deduced actin filament, tubulin, and software-deduced tubulin filament displayed, respectively. Actin staining delineates cell structure and coverage area. Scale bar = 50 μm for all images. (D)Violin plots illustrating statistics of morphological properties of cells plated on NC and hCOL3 conditions. (E) Angular probability distribution histogram displays actin filament angle from WB-F344 cells plated on NC or hCOL3 conditions. The bar graph displays the lengths of the same batches of actin filaments. n > 40 cells for all conditions in panels B and D. n > 10000 filaments for panel E.

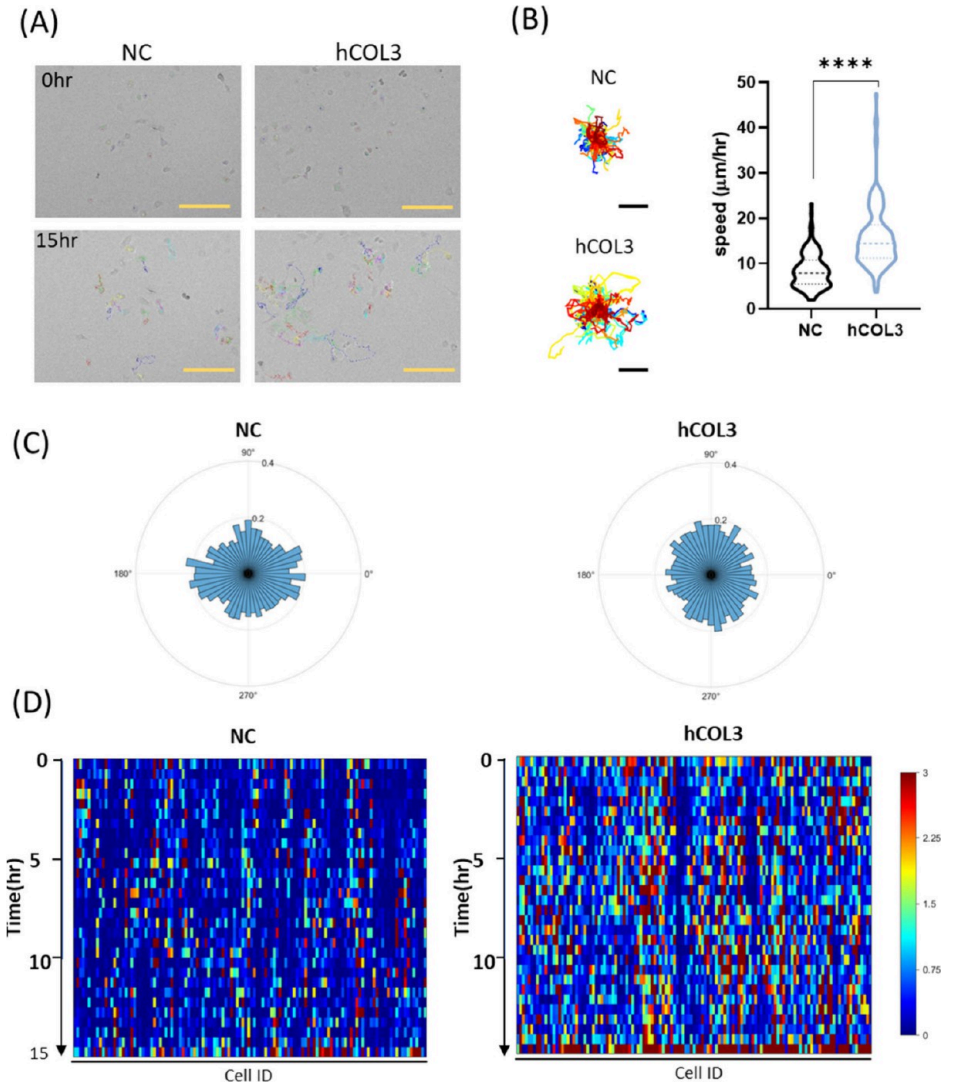

Figure 4. hCOL3 coating facilitates single-cell migration in cells. (A) Live imaging snapshots of single-cell migration at the beginning (0 h) and ending (15 h) of the experiment. Cells were plated on either NC or hCOL3 conditions; colored curves represent paths of cells migrating from the starting point. Scale bar = 200 μm for all images. (B) Migration paths for each condition within the 15 h translated such that the paths originate from the same point. The violin plot illustrates the statistics of time-mean speed, $\overline{v}$, for every cell whose migration paths were displayed on the left; each event in the graph represents $\overline{v}$ of a specific cell. Scale bar = 100 μm. n > 100 cells for each condition. (C) Instantaneous velocity direction angle distribution of single-cell migration for each condition. An angular probability distribution histogram is displayed, n > 3000 velocity vectors. (D) Kinetic energy density ($\frac{1}{2}\mathbf{v}^2$) heat map of single-cell migration. Each grid represents the KE density value of each cell at each time point of imaging (30 min interval within 0−15 h span). The vertical axis (oriented downward) represents time in hours, while the horizontal axis represents the number of each cell analyzed (from NO.1 to NO.n, where n > 100). KE density is expressed with unit k_BT/gram, and T = 37 °C (or 310 K), which applies to all other KE density heat maps in this research; Any value ≥ maximum in the color scale bar is displayed as the same color as the maximum (3 k_BT/gram in this case), which applies to all other KE density heat maps in this research.

structural dynamics of the cytoskeleton. The count of filopodium per cell was assessed using confocal microscopy images of the actin-stained channel. Filopodium count was adjusted for cells adjacent to other cells. The maximum number of adjacent cells of a particular cell was found to be 6 in all the images taken. Therefore, the corrected count of filopodia of a particular cell was evaluated as

$$N_c = \frac{N}{1 - \frac{N_a}{6}} \tag{20}$$

https://doi.org/10.1021/cbe.4c00133
Chem Bio Eng. 2025, 2, 97−109

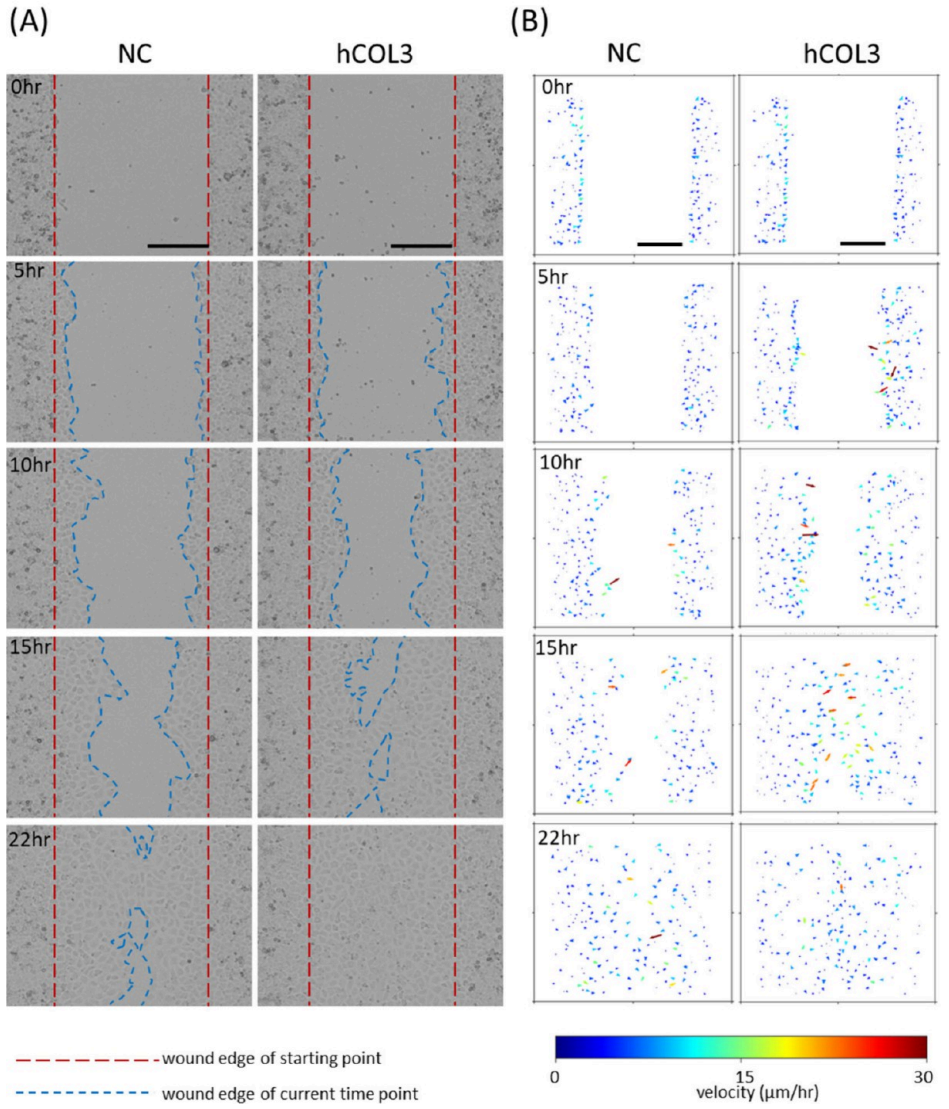

Figure 5. hCOL3 accelerated wound healing. (A) Live imaging snapshots documenting wound healing at 0 h (beginning), 5, 10, 15, and 22 h. Cells were plated on either NC or hCOL3 conditions. Dashed lines depict the initial wound edges (red) or wound edges at the indicated time points (blue). (B) Instantaneous velocity field of cells in the images presented in panel A, at the same time points and locations. For each arrow, the arrow end corresponds to the coordinates of the cell, the arrow length is proportional to the magnitude of the velocity, and the arrow direction is the same as the velocity direction. Any velocity norm ≥ the maximum in the color scale bar is depicted in the same color as the maximum (30 μm/h), which applies to all other vector field plots in this research. Scale bar = 200 μm for all images and plots in panels A and B.

where N is the filopodium count of the cell on edges not connecting with any other cell. N_a is the number of cells adjacent to the cell being evaluated (cells with 6 contacts are surrounded by other cells, and, therefore, cannot be evaluated for filopodia facing outside, so the denominator does not reach 0). N_c is the corrected filopodia count.

2.12. Statistical Method. Statistical analyses were conducted using two-tailed Student's t tests, with significance set at $p < 0.05$. * represents $0.01 < p < 0.05$; ** represents $0.001 < p < 0.01$; **** represents $p < 0.0001$. Plots typically display mean values ± SEM, with "n_{cells}" representing the number of filaments, cells, wells, or other events analyzed, which are specified in figure legends.

3. RESULTS

3.1. Design and Biosynthesis of Recombinant Human Collagen Type III. The biosynthesis of the hCOL3 was executed using two genetically modified host strains: *E. coli* ER2566 and *K. marxianus* CBS6556 (Figure 1). The comprehensive experimental methodologies are delineated in the methods section. The purity of the synthesized hCOL3 was confirmed by SDS-PAGE. Furthermore, mass spectrometry was used to verify the molecular weight and the amino acid sequence of hCOL3 (Table S3). Following these analyses, the purified hCOL3 was subjected to a series of biocompatibility assessments and validation procedures.

To assess the biocompatibility of hCOL3, we conducted a series of experiments focusing on cell viability, proliferation, and differentiation. Our results demonstrated that cells cultured in hCOL3-coated wells displayed growth rates, live/dead ratios, and proliferation indices that were comparable to those of a control group not treated with hCOL3 (Figure 2). Both RAW264.7 and WB-F344 cells exhibited around 90% viability. In an attempt to ascertain hCOL3's potential to induce differentiation in WB-F344 cells, we measured the expression

https://doi.org/10.1021/cbe.4c00133
Chem Bio Eng. 2025, 2, 97−109

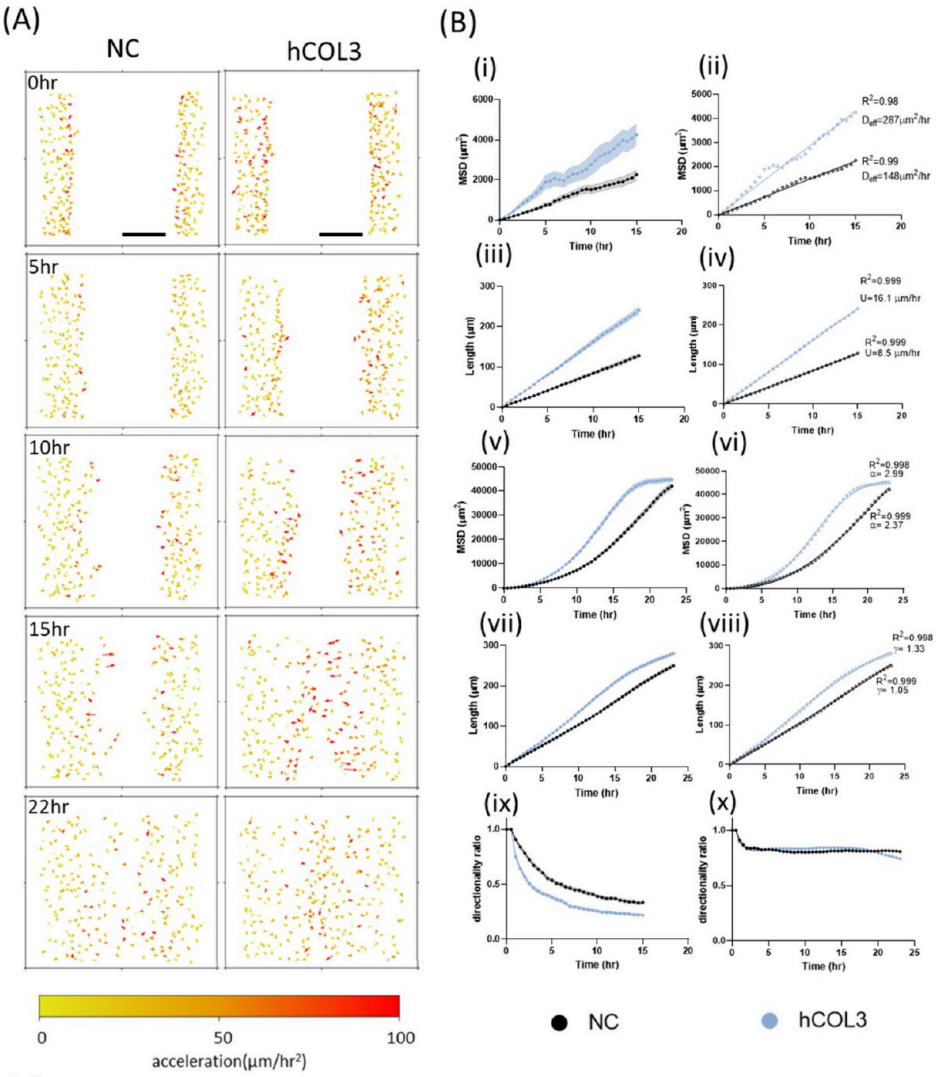

(C)

	Single Cell MSD	Single Cell Travel Length	Wound Healing MSD	Wound Healing Travel Length
NC	$D_{eff} = 148\mu m^2/hr$	$U = 8.5\ \mu m/hr$	$\alpha = 2.37$	$\gamma = 1.05$
hCOL	$D_{eff} = 287\mu m^2/hr$	$U = 16.1\ \mu m/hr$	$\alpha = 2.99$	$\gamma = 1.33$

Figure 6. Dynamic analyses of WB-F344 cell migration. (A) Instantaneous acceleration field of cells in the images presented in Figure 4A, at the same time points and locations. For each arrow, the arrow end corresponds to the coordinates of the cell, the arrow length is proportional to the magnitude of acceleration, and the arrow direction is consistent with the acceleration direction. Scale bar = 200 μm for all plots. (B) (i) MSD vs time plot of single-cell migration; (ii) model fitting of panel B(i); (iii) travel path length vs time plot of single-cell migration; (iv) model fitting of panel B(iii); (v) MSD vs time plot of wound healing; (vi) model fitting of panel B(v); (vii) travel path length vs time plot of wound healing; (viii) model fitting of panel B(vii); (ix) directionality ratio vs time plot of single-cell migration; (x) directionality ratio vs time plot of wound healing. (C) Table of representative physical parameters for fitted plots in panel B.

levels of liver lineage-specific markers. PCR analyses did not reveal any significant change in the expression of biliary markers, such as Yp and Aquaporin-1, or hepatocyte-specific genes, including albumin and glucose-6-phosphatase (G6 Pase), in cells treated with hCOL3, as depicted in Figure S1. Additionally, brightfield microscopy inspections did not detect any notable changes in the morphology. These findings collectively indicate that hCOL3 is biocompatible and supports fundamental cellular functions.

3.2. Effect of hCOL3 on Cell Morphology Deformation. Confocal microscopy analysis indicated that hCOL3 induced an increase in cell surface area and nuclear volume (Figure 3A,B). Cell circularity and aspect ratio remained relatively stable (Figure 3C,D). Treatment with hCOL3 substantially elongated actin filaments within the cells (Figure 3E and Figure S2). The elongation of actin filaments, in conjunction with the expansion of the cellular area, resulted in more pseudopodia extensions, suggesting a potential enhancement in the cells' ability to move in multiple directions.

3.3. hCOL3 Promotes Both Single-Cell and Collective-Migration. To analyze cell migration dynamics, we utilized two distinct assays: single-cell migration and collective-cell migra-

https://doi.org/10.1021/cbe.4c00133
Chem Bio Eng. 2025, 2, 97−109

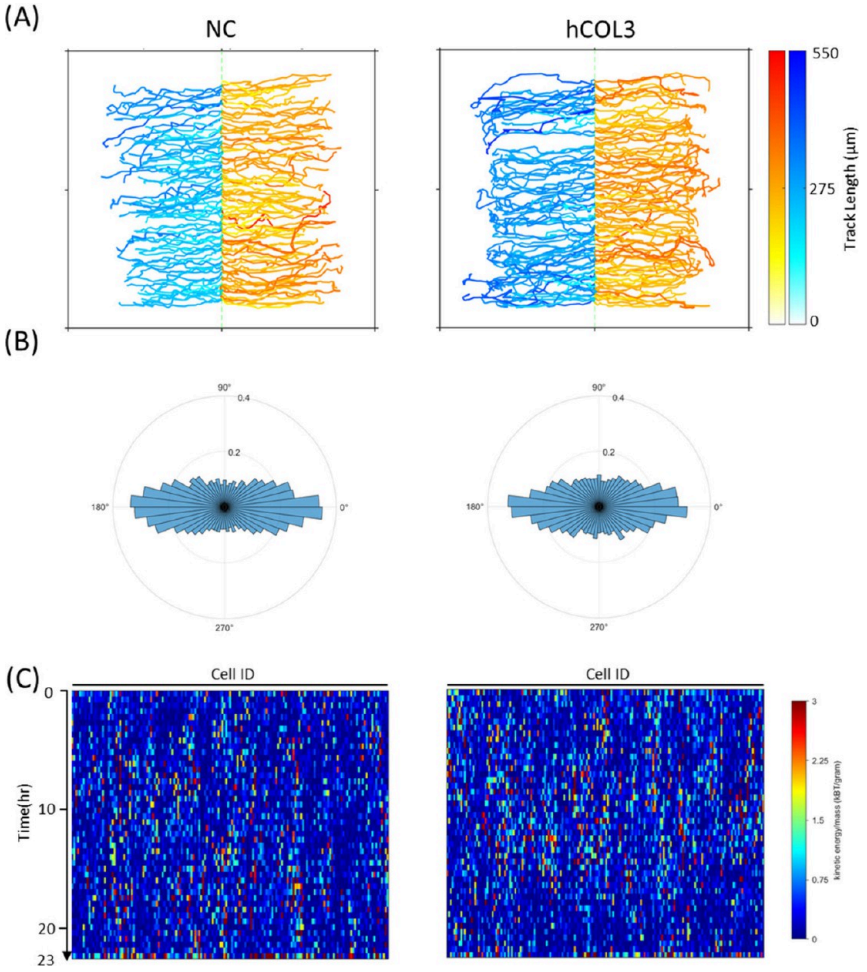

Figure 7. hCOL3-coating elongates leading cell path. (A) Migration paths of leading cells of wound healing within the 23 h were translated horizontally to the *y*-axis, such that the paths begin at coordinates (0,*y*), where *y* is the original *y*-coordinate where the paths begin. Paths moving leftward were colored cyan−blue, while those moving rightward were colored yellow−red. Any path length ≥ maximum in the color scale bar is depicted in the same color as the maximum (550 μm). (B) Instantaneous velocity direction angle distribution of leading cells of wound healing for both NC and hCOL3 conditions; angular probability distribution histogram is displayed; $n > 3000$ velocity vectors for each condition. (C) Kinetic energy density ($\frac{1}{2}\mathbf{v}^2$) heat map of wound healing leading cells.

tion. Single-cell migration, commonly modeled as a persistent **random walker or Brownian motion**, pertains to the movement of cells at low densities. In our study, WB-F344 exhibited elongated migration trajectories when cultured on substrates coated with hCOL3 (Figure 4). Mathematical analysis revealed that within the hCOL3 environment, physical parameters such as migration speed and effective diffusion coefficient D_{eff} were significantly elevated for WB-F344 cells (Figures 4, 5, and 6). On the hCOL3-coated surface, the single-cell migration speed of WB-F344 was increased from 8.5 μm/h to 16.1 μm/h, and D_{eff} was elevated from 148 μm^2/h to 287 μm^2/h (Figures 4, 5, and 6). Moreover, the directionality ratio, a measure of the displacement from the starting point relative to the total distance traveled, diminished over time and was constantly lower in hCOL3 than in the NC group. This decrease suggests that randomness increases as cell movement proceeds, and the hCOL3 coating introduces a greater element of randomness into cell movement.

Collective cell migration was assessed using a wound-healing assay. Consistent with our single-cell findings, the collective migration rate of WB-F344 cells was markedly enhanced on hCOL3-coated substrates, resulting in accelerated wound closure (Figure 5). Cells at the forefront of the wound-healing process (leading cell) on hCOL3-coated surfaces exhibited elongated migration paths and an earlier concentration of kinetic energy compared to those on NC surfaces (Figure 7). The migration trajectories deviated from the typical random walk, instead aligning with superdiffusion or hyperballistic diffusion patterns. The mean squared displacement (MSD) as a function of time, expressed as $\langle r^2(t)\rangle = At^{\alpha}$, where A is an empirical coefficient, characterizing different types of particle motion: $\alpha < 1$ indicates subdiffusion, $\alpha = 1$ represents normal diffusion observed in the long term for single-cell motion, $1 < \alpha < 2$ signifies superdiffusion, and $\alpha > 2$ denotes hyperballistic diffusion. Cases where $\alpha > 2$ imply the presence of a momentum field. The MSD data from leading cells were plotted over time and adjusted to a model that takes into consideration the asymptotic phase of wound healing (Figure 6).

$$\langle \mathbf{r}^2(t)\rangle = R_C{}^2[1 - e^{-A/R_C{}^2 t^{\alpha}}]$$

3.4. Comparison of Dynamics between Single-Cell and Collective-Cell Migration. Analysis of collective cell migration utilizing a wound-healing model elucidated distinct migration dynamics between noncoated and hCOL3-coated

https://doi.org/10.1021/cbe.4c00133
Chem Bio Eng. 2025, 2, 97−109

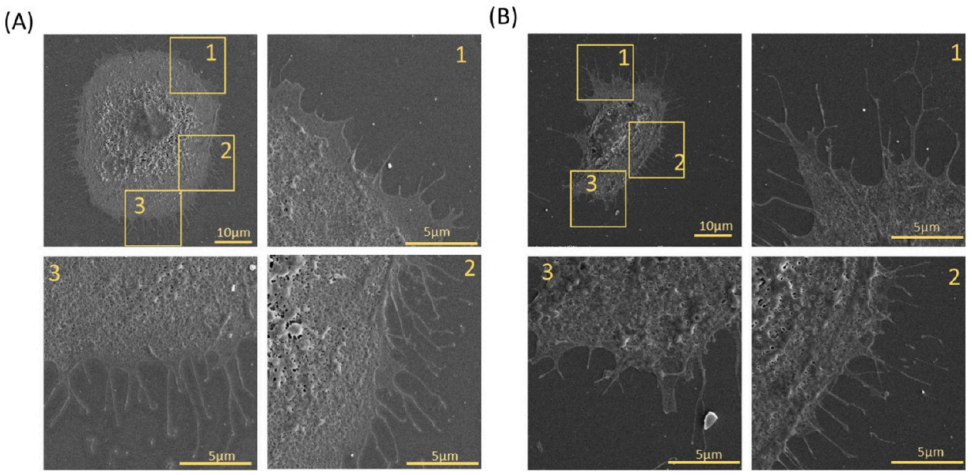

Figure 8. hCOL3-coating promoting the formation of filopodia. SEM images of WB-F344 cells plated on NC (A) and hCOL3 (B) substrates at various magnifications. In each condition, the image at the upper-left corner displays an entire cell, while the other three images are magnified views of portions enclosed within each yellow frame, labeled with corresponding numbers. Scale bar values are indicated on the images.

conditions. The power-law exponent of MSD, α, derived from fitting the data, was 2.37 for NC and notably higher at 2.99 for the hCOL3-coated condition. Likewise, the power-law exponent of travel path length, γ, was 1.05 for NC and notably higher at 1.33 for hCOL3 (Figure 6B,C). The increase in the exponents suggests that hCOL3 amplifies the rate of mean squared displacement (MSD), pointing to a migration that is both more directed and rapid. Unlike in single-cell migration, where hCOL3 introduction was linked to an increase in chaotic motion, the directionality curves for leading cells during wound healing under NC and hCOL3 conditions exhibited substantial overlap (Figure 6B). This similarity indicates that hCOL3 does not engender a chaotic migration pattern within the context of collective cell movements. Furthermore, an in-depth examination of velocity and acceleration vector fields across all cells under hCOL3 conditions revealed a higher frequency of high-velocity and high-acceleration events (Figures 5, 6, and 7). The augmented momentum field associated with hCOL3 may be a contributing factor to the more efficient wound closure. These results underscore the potential utility of hCOL3 as a substrate for enhancing collective cell migration.

3.5. Number and Length of Filopodia during Cell Migration. The use of scanning electron microscopy (SEM) has provided detailed insights into the pseudopods of WB-F344 cells. SEM imaging at lower magnifications revealed the cells to be elliptical, while higher magnifications exposed the intricate presence of filopodia, filamentous pseudopods (as shown in Figures 8, and 9). Notably, cells cultured on glass substrates coated with hCOL3 displayed a greater number of filopodia compared to those on NC surfaces. This increase in both the number and length of filopodia in hCOL3-treated cells is consistent with the observed elongation of actin filaments, as depicted in Figures 8 and 9. Furthermore, the hCOL3 coating seemed to promote a dendritic pattern in the distribution of filopodia, characterized by increased branching and a higher number of branching points (Figures 8 and 9). Throughout the migration phase, these leading cells used their filopodia to connect with follower cells, effectively guiding them toward the moving site. The development of fan-shaped pseudopodia during the migration of leading cells highlights the directed nature of collective cell migration, facilitated by both filopodial elongation and the extension of other pseudopod types.

Filopodial number and length are pivotal to cell migration, influencing both the velocity and directionality of movement. As thin, actin-rich protrusions, filopodia are integral to a cell's exploratory interactions with ECM. An increased filopodial count enhances a cell's capacity to detect environmental cues, while longer filopodia extend the cell's reach, enabling a more robust response to these stimuli. Filopodia act as pioneers in cell migration, guiding the cell's trajectory by forming transient attachments with the ECM, which generate the traction forces necessary for cell body advancement. The dynamic assembly and disassembly of filopodia contribute to the adaptability of cell movement, allowing cells to navigate complex environments and adjust their migration path in response to dynamic conditions.

4. DISCUSSION

Collagen is the main component of the extracellular matrix (ECM)[26] accounting for about 30% of the total protein content of the human body, 70% of the dry weight of human skin, 80% of organic matter in bone, and about 90% of human tendon and corneal tissue.[27] The collagen family has 28 members with high diversity since each type has unique molecular isomers.[28] This molecular diversity contributes to the variation in physical and chemical properties as this protein condensates into solid matter. Collagen regulates several intrinsic and extrinsic signaling pathways generally involving development, regeneration, and repair to ensure tissue homeostasis.[29] The interaction of collagen with biological cells is mainly facilitated by specific receptors that can bidirectionally transmit mechanical or biochemical signals by cytoskeleton-mediated mechanosensory and mechanotransduction.[29,30]

Cell migration is significantly influenced by the presence of collagen, a fundamental component of the ECM, which provides both structural support and biochemical signaling.[31] Cells sense collagen through a process known as durotaxis, which is essential for migration due to the ECM's role in focal adhesion formation. These adhesions are vital for linking the cell's cytoskeleton to the collagen-rich ECM, thereby facilitating the transmission of mechanical signals that propel cell motility. The actin cytoskeleton is particularly sensitive to collagen fiber density, affecting the dynamics of actin filament assembly and disassembly, which are crucial for cell protrusion and migration. SEM of WB-F344 has elucidated the role of filopodia in cell

https://doi.org/10.1021/cbe.4c00133
Chem Bio Eng. 2025, 2, 97−109

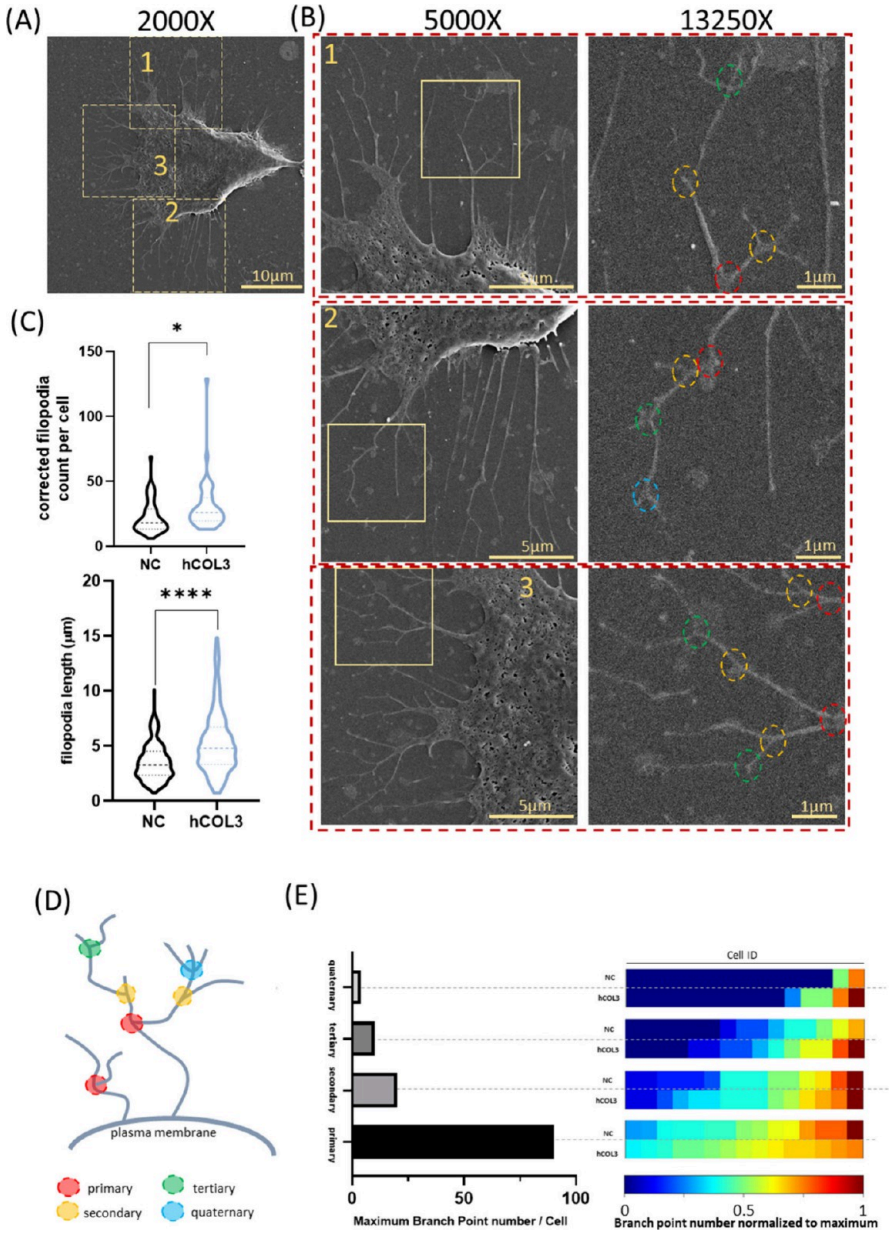

Figure 9. hCOL3-coating promoting the formation of longer and more dendritic filopodia in cells. (A) SEM image of an authentic WB-F344 cell with filopodia exhibiting various ranks of dendritic branches. The image is at 2000× magnification. (B) Magnified views of the image in panel A: The 5000× images in the first column are magnified views of the portions enclosed in the yellow boxes depicted in panel A, labeled with corresponding numbers. The 13250× images in the second column are further magnified portions within the numbered frames depicted in the corresponding 5000× images in the first column. The nomenclature of dashed line circles with different colors on branch points is defined in the cartoon in panel D. (C) Violin plots of the corrected filopodia count per cell and filopodia length in both conditions. $n > 30$ cells in filopodia count plot, and $n > 300$ filopodia in length plot. (D) Cartoon illustrating the nomenclature of primary to quaternary rankings of branch points of filopodia, with authentic branch points marked with dashed-line circles in the 13250× images in panel B. (E) Bar graph (left) and heat map (right) depicting the maximum number of branch points for each rank observed in cells plated on both NC and hCOL3 substrates. The left bar graph illustrates the maximum number of branch points of a particular rank observed in all of the cells analyzed (in both NC and hCOL3 conditions). Ten cells in each condition were analyzed. Each grid on the heat map represents the normalized number of cellular branch points of a particular rank relative to the maximum displayed on the left. The actual number of cellular branch points of a rank is expressed as the maximum value on the left multiplied by the normalized ratio on the right.

migration, especially in the context of wound healing. SEM imaging at lower magnifications reveals the elliptical cell shape, while higher magnifications highlight the presence of delicate, filamentous filopodia. Cells cultured on surfaces coated with hCOL3 demonstrate a significant increase in both the number and length of filopodia compared to those on noncoated surfaces.

The hCOL3 coating not only enhances the quantity and length of filopodia but also promotes a dendritic distribution pattern, characterized by increased branching and a higher number of branching points. This pattern suggests a more complex and potentially more effective migratory behavior. In the context of wound healing, leading cells at the wound edge initially exhibit sparse filopodia, aligned toward the wound, indicating the direction of healing. These cells use filopodia to

https://doi.org/10.1021/cbe.4c00133
Chem Bio Eng. 2025, 2, 97−109

connect with follower cells, effectively guiding them toward the moving site. The development of fan-shaped pseudopodia during the migration of leading cells underscores the directed nature of collective cell migration, facilitated by filopodial elongation and the extension of other pseudopod types.

Filopodial number and length are critical for cell migration, affecting both the velocity and directionality of movement. As thin, actin-rich protrusions, filopodia are integral to a cell's exploratory interactions with the ECM. An increased filopodial count enhances a cell's ability to detect environmental cues, such as the presence of collagen, while longer filopodia extend the cell's reach, enabling a more robust response to these stimuli. Filopodia act as pioneers in cell migration, guiding the cell's trajectory by forming transient attachments with the ECM, which generate the traction forces necessary for cell body advancement. The dynamic assembly and disassembly of filopodia contribute to the adaptability of cell movement, allowing cells to navigate complex environments and adjust their migration path in response to dynamic conditions.

In conclusion, the SEM analysis of WB-F344 cells on hCOL3-coated surfaces has shed light on the intricate relationship between filopodia and cell migration. The increased filopodial number and length, along with the dendritic pattern of distribution, suggest a more efficient migratory behavior essential for wound healing. The role of filopodia in guiding cell movement, detecting environmental cues, and generating traction forces for cell body advancement is paramount. These findings highlight the potential therapeutic applications of hCOL3 in promoting cellular dynamics advantageous for tissue repair and wound healing. This research initially demonstrates the dynamic analysis of pseudopodia-driven cell migration induced by collagen, providing a foundation for future biomedical engineering.

■ ASSOCIATED CONTENT

Data Availability Statement

The data sets generated during the current study are available from the corresponding author upon reasonable request.

Supporting Information

The Supporting Information is available free of charge at https://pubs.acs.org/doi/10.1021/cbe.4c00133.

Summary of strains, plasmid, primers for cloning, and gene sequence in this study (PDF)

■ AUTHOR INFORMATION

Corresponding Authors

Yuan Yao − *ZJU-Hangzhou Global Scientific and Technological Innovation Center, Zhejiang University, Hangzhou, Zhejiang 311200, China; College of Chemical and Biological Engineering, Zhejiang University, Hangzhou, Zhejiang 310027, China;* orcid.org/0000-0001-5262-5115; Email: yyao1@zju.edu.cn

Xuye Lang − *ZJU-Hangzhou Global Scientific and Technological Innovation Center, Zhejiang University, Hangzhou, Zhejiang 311200, China; College of Chemical and Biological Engineering, Zhejiang University, Hangzhou, Zhejiang 310027, China*; Email: xuyelang@zju.edu.cn

Ming Li − *Department of Dermatology, Children's Hospital of Fudan University, National Children's Medical Center, Shanghai 201102, China*; Email: mingli@fudan.edu.cn

Authors

Ruiwen Fu − *ZJU-Hangzhou Global Scientific and Technological Innovation Center, Zhejiang University, Hangzhou, Zhejiang 311200, China; College of Chemical and Biological Engineering, Zhejiang University, Hangzhou, Zhejiang 310027, China*

Kuangzheng Zhu − *Zhejiang Lab, Hangzhou, Zhejiang 311121, China*

Zhouyang Li − *ZJU-Hangzhou Global Scientific and Technological Innovation Center, Zhejiang University, Hangzhou, Zhejiang 311200, China*

Liqun Lei − *The First Affiliated Hospital, Zhejiang University School of Medicine, Hangzhou, Zhejiang 311100, China*

Complete contact information is available at: https://pubs.acs.org/10.1021/cbe.4c00133

Author Contributions

#R.F., K.Z., Z.L., and L.L. contributed equally to this work. Y.Y. and X.L. designed the study, analyzed the data, and wrote the manuscript. M.L., R.F., K.Z., Z.L., and L.L. conducted the experiments. All authors revised and approved the manuscript.

Notes

The authors declare no competing financial interest.

■ ACKNOWLEDGMENTS

This work was partially supported by grants from the National Natural Science Foundation of China General Program (Grant No. 32071347 to Y.Y.), the National Key R&D Program of China (Grant No. 2023YFC3402402 to Y.Y.), the Zhejiang Lab Open Research Project as China Computer Federation (CCF)—Zhejiang Lab Research Project (Grant No. K2022PE0AB08 to Y.Y.), the Zhejiang Provincial Natural Science Foundation of China (Grant No. ZCLQ24C0101 to X.L.), ZJU-Hangzhou Global Scientific and Technological Innovation Center, Zhejiang University (Grant Nos. 02020200-K02013008 to Y.Y. and 02020200-K02013027 to X.L.), Jiangsu Wuzhong Aesthetics Biotech Co., Ltd. (Grant No. XS-KF-2022-0098 to Y.Y.), and the Fundamental Research Funds for the Central Universities (226-2022-00214). Also acknowledged is the support of the ZJU-Hangzhou Global Scientific and Technological Innovation Center, Zhejiang University (HIC-ZJU), the *i*Biofoundary, the Core Facility of the Institute for Intelligent Bio/Chem Manufacturing at HIC-ZJU.

■ REFERENCES

(1) Trepat, X.; Chen, Z.; Jacobson, K. Cell Migration. In *Comprehensive Physiology*; Prakash, Y. S., Ed.; Wiley, 2012; pp 2369−2392. DOI: 10.1002/cphy.c110012.

(2) Vercruysse, E.; Brückner, D. B.; Gómez-González, M.; Remson, A.; Luciano, M.; Kalukula, Y.; Rossetti, L.; Trepat, X.; Hannezo, E.; Gabriele, S. Geometry-Driven Migration Efficiency of Autonomous Epithelial Cell Clusters. *Nat. Phys.* **2024**, *20*, 1492.

(3) Alert, R.; Trepat, X. Physical Models of Collective Cell Migration. *Annu. Rev. Condens. Matter Phys.* **2020**, *11* (1), 77−101.

(4) SenGupta, S.; Parent, C. A.; Bear, J. E. The Principles of Directed Cell Migration. *Nat. Rev. Mol. Cell Biol.* **2021**, *22* (8), 529−547.

(5) Novikov, N. M.; Zolotaryova, S. Y.; Gautreau, A. M.; Denisov, E. V. Mutational Drivers of Cancer Cell Migration and Invasion. *Br. J. Cancer* **2021**, *124* (1), 102−114.

(6) García-Cuesta, E. M.; Santiago, C. A.; Vallejo-Díaz, J.; Juarranz, Y.; Rodríguez-Frade, J. M.; Mellado, M. The Role of the CXCL12/CXCR4/ACKR3 Axis in Autoimmune Diseases. *Front Endocrinol (Lausanne)* **2019**, *10*, 585.

(7) Glass, D. S.; Grossfeld, D.; Renna, H. A.; Agarwala, P.; Spiegler, P.; Kasselman, L. J.; Glass, A. D.; DeLeon, J.; Reiss, A. B. Idiopathic Pulmonary Fibrosis: Molecular Mechanisms and Potential Treatment Approaches. *Respir Investig* **2020**, *58* (5), 320−335.
(8) Shekhter, A. B.; Fayzullin, A. L.; Vukolova, M. N.; Rudenko, T. G.; Osipycheva, V. D.; Litvitsky, P. F. Medical Applications of Collagen and Collagen-Based Materials. *Curr. Med. Chem.* **2019**, *26* (3), 506−516.
(9) Wang, W.; Lin, S.; Xiao, Y.; Huang, Y.; Tan, Y.; Cai, L.; Li, X. Acceleration of Diabetic Wound Healing with Chitosan-Crosslinked Collagen Sponge Containing Recombinant Human Acidic Fibroblast Growth Factor in Healing-Impaired STZ. Diabetic Rats. *Life Sci.* **2008**, *82* (3−4), 190−204.
(10) Riching, K. M.; Cox, B. L.; Salick, M. R.; Pehlke, C.; Riching, A. S.; Ponik, S. M.; Bass, B. R.; Crone, W. C.; Jiang, Y.; Weaver, A. M.; Eliceiri, K. W.; Keely, P. J. 3D Collagen Alignment Limits Protrusions to Enhance Breast Cancer Cell Persistence. *Biophys. J.* **2014**, *107* (11), 2546−2558.
(11) Fraley, S. I.; Wu, P.-H.; He, L.; Feng, Y.; Krisnamurthy, R.; Longmore, G. D.; Wirtz, D. Three-Dimensional Matrix Fiber Alignment Modulates Cell Migration and MT1-MMP Utility by Spatially and Temporally Directing Protrusions. *Sci. Rep* **2015**, *5*, No. 14580.
(12) Sapudom, J.; Rubner, S.; Martin, S.; Kurth, T.; Riedel, S.; Mierke, C. T.; Pompe, T. The Phenotype of Cancer Cell Invasion Controlled by Fibril Diameter and Pore Size of 3D Collagen Networks. *Biomaterials* **2015**, *52*, 367−375.
(13) Clark, A. G.; Maitra, A.; Jacques, C.; Bergert, M.; Pérez-González, C.; Simon, A.; Lederer, L.; Diz-Muñoz, A.; Trepat, X.; Voituriez, R.; Vignjevic, D. M. Self-Generated Gradients Steer Collective Migration on Viscoelastic Collagen Networks. *Nat. Mater.* **2022**, *21* (10), 1200−1210.
(14) Li, W.; Chi, N.; Rathnayake, R. A. C.; Wang, R. Distinctive Roles of Fibrillar Collagen I and Collagen III in Mediating Fibroblast-Matrix Interaction: A Nanoscopic Study. *Biochem. Biophys. Res. Commun.* **2021**, *560*, 66−71.
(15) Condeelis, J. Life at the Leading Edge: The Formation of Cell Protrusions. *Annu. Rev. Cell Biol.* **1993**, *9*, 411−444.
(16) Parent, C. A.; Blacklock, B. J.; Froehlich, W. M.; Murphy, D. B.; Devreotes, P. N. G Protein Signaling Events Are Activated at the Leading Edge of Chemotactic Cells. *Cell* **1998**, *95* (1), 81−91.
(17) Chodniewicz, D.; Zhelev, D. V. Novel Pathways of F-Actin Polymerization in the Human Neutrophil. *Blood* **2003**, *102* (6), 2251−2258.
(18) Zigmond, S. H. Ability of Polymorphonuclear Leukocytes to Orient in Gradients of Chemotactic Factors. *J. Cell Biol.* **1977**, *75* (2), 606−616.
(19) Holly, S. P.; Larson, M. K.; Parise, L. V. Multiple Roles of Integrins in Cell Motility. *Exp. Cell Res.* **2000**, *261* (1), 69−74.
(20) Millard, T. H.; Martin, P. Dynamic Analysis of Filopodial Interactions during the Zippering Phase of Drosophila Dorsal Closure. *Development* **2008**, *135* (4), 621−626.
(21) Jacquemet, G.; Hamidi, H.; Ivaska, J. Filopodia in Cell Adhesion, 3D Migration and Cancer Cell Invasion. *Curr. Opin Cell Biol.* **2015**, *36*, 23−31.
(22) Wood, W.; Jacinto, A.; Grose, R.; Woolner, S.; Gale, J.; Wilson, C.; Martin, P. Wound Healing Recapitulates Morphogenesis in Drosophila Embryos. *Nat. Cell Biol.* **2002**, *4* (11), 907−912.
(23) Woolner, S.; Jacinto, A.; Martin, P. The Small GTPase Rac Plays Multiple Roles in Epithelial Sheet Fusion–Dynamic Studies of Drosophila Dorsal Closure. *Dev. Biol.* **2005**, *282* (1), 163−173.
(24) Tobin, M. P.; Pfeifer, C. R.; Zhu, P. K.; Hayes, B. H.; Wang, M.; Vashisth, M.; Xia, Y.; Phan, S. H.; Belt, S. A.; Irianto, J.; Discher, D. E. Differences in Cell Shape, Motility, and Growth Reflect Chromosomal Number Variations That Can Be Visualized with Live-Cell ChReporters. *MBoC* **2023**, *34* (13), No. br19.
(25) Gorelik, R.; Gautreau, A. Quantitative and Unbiased Analysis of Directional Persistence in Cell Migration [J]. *Nat. Protoc* **2014**, *9* (8), 1931−43.
(26) Granito, R. N.; Custódio, M. R.; Rennó, A. C. M. Natural Marine Sponges for Bone Tissue Engineering: The State of Art and Future Perspectives. *J. Biomed Mater. Res.* **2017**, *105* (6), 1717−1727.
(27) Viguet-Carrin, S.; Garnero, P.; Delmas, P. D. The Role of Collagen in Bone Strength. *Osteoporos Int.* **2006**, *17* (3), 319−336.
(28) Ricard-Blum, S. The Collagen Family. *Cold Spring Harbor Perspectives in Biology* **2011**, *3* (1), a004978−a004978.
(29) Elango, J.; Hou, C.; Bao, B.; Wang, S.; Maté Sánchez De Val, J. E.; Wenhui, W. The Molecular Interaction of Collagen with Cell Receptors for Biological Function. *Polymers* **2022**, *14* (5), 876.
(30) Hu, K.; Hu, M.; Xiao, Y.; Cui, Y.; Yan, J.; Yang, G.; Zhang, F.; Lin, G.; Yi, H.; Han, L.; Li, L.; Wei, Y.; Cui, F. Preparation Recombination Human-like Collagen/Fibroin Scaffold and Promoting the Cell Compatibility with Osteoblasts. *J. Biomedical Materials Res.* **2021**, *109* (3), 346−353.
(31) Monzo, P.; Chong, Y. K.; Guetta-Terrier, C.; Krishnasamy, A.; Sathe, S. R.; Yim, E. K. F.; Ng, W. H.; Ang, B. T.; Tang, C.; Ladoux, B.; Gauthier, N. C.; Sheetz, M. P. Mechanical Confinement Triggers Glioma Linear Migration Dependent on Formin FHOD3. *MBoC* **2016**, *27* (8), 1246−1261.

https://doi.org/10.1021/cbe.4c00133
Chem Bio Eng. 2025, 2, 97−109